Available online at www.sciencedirect.com

ScienceDirect

Publishing Services by Elsevier

International Journal of Naval Architecture and Ocean Engineering 10 (2018) 307–317
http://www.journals.elsevier.com/international-journal-of-naval-architecture-and-ocean-engineering/

# Numerical investigations of tip clearance flow characteristics of a pumpjet propulsor

Lin Lu [a,*], Yuefei Gao [a], Qiang Li [a], Lin Du [b]

[a] School of Mechatronic Engineering, North University of China, Taiyuan 030051, China
[b] College of Engineering, Florida Institute of Technology, Melbourne, FL 32901, USA

Received 27 May 2017; revised 27 August 2017; accepted 3 September 2017
Available online 30 September 2017

**Abstract**

In this study, numerical investigations of the tip clearance flow characteristics of a pumpjet propulsor based on Computational Fluid Dynamics (CFD) method have been presented. The Zwart-Gerber-Belamri (Z-G-B) cavitation model based on Reynolds Averaged Navier–Stokes (RANS) method is employed. The structured gird is applied. The formation and development of the tip clearance flows has been investigated and presented. The structure of the tip leakage vortex has been shown. The radial distributions of different velocity components with different Span along the axial direction have been carried out to present the influence of the tip clearance flow on the main flow. In addition, the influences of the tip clearance size on the pumpjet propulsor performance, including the impact on the velocity flow fields and the cavitation characteristic, have been presented.


*Keywords:* Pumpjet propulsor; Numerical investigation; Tip clearance characteristic; Tip leakage vortex; Tip clearance size

## 1. Introduction

The propulsion system is an important part of underwater vehicle, which has a direct impact on the quality and performance of the vehicle. The pumpjet propulsor has the advantages of high efficiency, low radiation noise and high rotational speed and has been widely applied in both military and commercial fields. However, present literature review suggests that the numerical simulation of the hydrodynamics and cavitation performance of pumpjet propulsor is few and far between, especially the investigation of tip clearance flow characteristics of pumpjet propulsor is even less. With the rapid development of computational methods, Computational Fluid Dynamics (CFD) method has become more and more practical and reliable for the investigation of tip clearance flow characteristics of pumpjet propulsor.

A number of experimental and numerical investigations of flow characteristics on the waterjet propeller, axial-flow pump and conventional marine propeller have been carried out and obtained some useful and reliable results that are of benefit to advance in research of flow characteristics of pumpjet propulsor. For non-cavitating flow condition, Park et al. (2005) carried out the numerical simulations of a waterjet propulsion system to provide detail understanding of complicated three-dimensional viscous flow phenomena. Cheah et al. (2007) simulated the complex internal flow in a centrifugal pump impeller with six twisted blades by using a 3D Navier–Stokes code with a standard $k-\varepsilon$ turbulence model. Results showed the development of flows and the flow pattern of separation precisely. Zhang et al. (2010) presented the 3D unsteady turbulent flow in axial-flow pumps. Numerical results showed that the unsteady prediction results were more accurate than the steady results. Besides, the static pressure fluctuation had been investigated. Rhee and Joshi (2005) presented the results of CFD validation for flow around a marine propeller. The overall results suggested that the present approach

* Corresponding author.
*E-mail address:* lulin2016@nuc.edu.cn (L. Lu).
Peer review under responsibility of Society of Naval Architects of Korea.

http://dx.doi.org/10.1016/j.ijnaoe.2017.09.001

was practicable for actual propeller design procedures. Muscari and Di Mascio (2011) developed the numerical simulations of the flow past a rotating propeller behind a hull. The numerical data was verified and validated by comparing with measurements. Ivanell (2001) described a CFD model of the pumpjet propulsor on a torpedo using FLUENT to verify its accuracy by comparing numerical simulation results with wind tunnel experiments. It could be concluded from the simulations that the result for propulsion force is about 10% higher when compared with measurements. Suryanarayana et al. (2010a,b,c) carried out the numerical and experimental investigations of a pumpjet propulsor on an underwater body. Results suggested that the CFD method turned out to be useful and economical method for quick assessment of overall performance of the propulsor and generation of exhaustive fluid dynamic data. For cavitating flow condition, Lindau et al. (2005) applied a 3D multiphase RANS computational tool to predict the propeller load for a designated propeller. The critical cavitation number for the thrust and torque breakdown is predicted and agreed well with the experimental data over a wide range of modeled flow coefficients. Shin (2010) applied a mixed multiphase flow model and a 3D RANS method to predict the hydrodynamic and cavitation performance of typical marine propeller cavitation. Morgut and Nobile (2012) used a commercial CFD code to numerically calculate and discuss the cavitating flow around two model scale propellers in uniform inflow. The numerical results were close to the experimental data, while a tendency to overestimate the cavity extension was observed. Zhu and Fang (2012) used the full cavitation model to predict N–S equation for the 3D cavitating flow of two typical marine propellers. The numerical simulation results of the cavitation and hydrodynamic performance of two propellers agreed with the experimental results. Brennen (2013) presented a review of some of the recent developments in our understanding of the dynamics and instabilities caused by cavitation in pumps. Ji et al. (2014a,b) simulated unsteady cavitation characteristics and alleviation of pressure fluctuations around two marine propellers in the non-uniform wake. Luo et al. (2016) mainly summarized the recent progresses for the cavitation study in the hydraulic machinery including turbo-pumps, hydro turbines, etc. Ji et al. (2014a,b, 2015, 2017) studied the cavitating flow around a NACA66 hydrofoil numerically with particular emphasis on understanding the cavitation structures and the shedding dynamics based on Large Eddy Simulation (LES). Suryanarayana et al. (2010a,b) presented experimental investigations on an axi-symmetric body model fitted with pumpjet propulsor in cavitation tunnel. The results were found to match closely with the towing tank results.

## 2. Numerical investigation method

### 2.1. Governing equation

For the three-dimensional incompressible and single-phase fluid, the viscous flow theory is applied to solve the Reynolds Averaged Navier–Stokes (RANS) equation, and the governing equation can be written as follows:

$$\frac{\partial \overline{u}_i}{\partial x_i} = 0 \tag{1}$$

$$\rho\frac{\partial \overline{u}_i}{\partial t} + \rho\overline{u}_j\frac{\partial \overline{u}_i}{\partial x_j} = \rho\overline{F}_i - \frac{\partial \overline{p}}{\partial x_i} + \frac{\partial}{\partial x_j}\left(\mu\frac{\partial \overline{u}_i}{\partial x_j} - \rho\overline{u_i'u_j'}\right) \tag{2}$$

where $i = 1, 2, 3, j = 1, 2, 3$, $\rho$ denotes the fluid density, and $x_i$ and $x_j$ are the Cartesian coordinate components. $F$ is the body force on the micro element. $\mu$ and $p$ represent the dynamic viscosity and the pressure, respectively. $u_i$ and $u_j$ are the absolute velocity. $\rho\overline{u_i'u_j'}$ depicts the Reynold stress. When the cavitation phenomenon occurs, the governing equations are the same as Eqs. (1) and (2) of a single phase fluid, except that the fluid density $\rho$ used in Eqs. (1) and (2) need to be replaced with the expression of the mixture density and $\rho_m$.

$$\rho_m = \alpha_v\rho_v + (1-\alpha_v)\rho_l \tag{3}$$

where $\alpha_v$ and $\rho_v$ denote the vapor volume fraction and density, respectively. $\rho_l$ represents the liquid density.

### 2.2. Cavitation model

According to the available research data (Singhal et al., 2002; Watanabe et al., 2003; Arazgaldi et al., 2009; Salvatore et al., 2009), the most widely used cavitation model for the numerical simulation of marine propeller's cavitating flows is the Singhal cavitation model that is also known as the full cavitation model. However, the Singhal cavitation model is physically incorrect and numerically unstable if applied to evaporation. The fundamental reason is that one of the key assumptions is that the cavitation bubble does not interact with each other. This is plausible only during the earliest stage of cavitation when the cavitation bubble grows from the nucleation stage. As the vapor volume fraction increases, the nucleation site density must decrease accordingly. To modify this process, the Zwart-Gerber-Belamri cavitation model in commercial code ANSYS CFX (2012) has been applied in this study, and it replaces $\alpha_v$ in the Singhal cavitation model with $\alpha_{nuc}(1-\alpha_v)$, $\alpha_{nuc}$ depicts nucleation site volume fraction and equals to $5\times10^{-4}$. Then the final form of this cavitation model is written as follows:

$$R_e = F_{vap}\frac{3\alpha_{nuc}(1-\alpha_v)\rho_v}{R_B}\sqrt{\frac{2}{3}\frac{(p_v-p)}{\rho_l}} \tag{4}$$

$$R_c = F_{cond}\frac{3\alpha_v\rho_v}{R_B}\sqrt{\frac{2}{3}\frac{(p_v-p)}{\rho_l}} \tag{5}$$

where $R_e$ and $R_c$ represent the vaporization and condensation rates per unit volume, respectively. The radius of a vapor bubble is $R_B = 10^{-6}$ m. The evaporation coefficient $F_{vap} = 50$ and the condensation coefficient is $F_{cond} = 0.01$. $p_v$ and $p$

represent the saturation vapor pressure and the pressure in the fluid surrounding the bubble, respectively.

In addition, based on the research data by Ji et al. (2010), the SST $k-\omega$ turbulence model can accurately predict the initiation of the flows and the flow separation quantity under the condition of negative pressure gradient with better practicability and reliability. Thus, the SST $k-\omega$ turbulence model is adopted for the numerical predictions in this study.

## 3. Tip clearance flow characteristics of a pumpjet propulsor

### 3.1. Numerical method verification

In order to verify the accuracy of numerical simulation method in this study, the numerical simulations of the steady non-cavitating and cavitating flows over a skewed four-bladed marine propeller E779A have been carried out. E779A propeller has been widely studied and tested for several years. The reliable experimental data is available by Li et al. (2012) and Liu et al. (2012). The specific simulations and calculations details of E779A propeller have been presented in our previous research papers (Pan and Lu, 2016; Lu et al., 2016). The main parameters of E779A propeller are shown as Table 1. The computational grid of E779A propeller is presented in Fig. 1.

### 3.2. Computational model and boundary conditions

In this study, a pumpjet propulsor with the full hydraulic passage has been applied for the computational model of numerical prediction, as shown in Fig. 2. The main parameters of the pumpjet propulsor are listed in Table 2. Besides, one hemispherical flow-guide is installed in the front of the rotor blade and the other is fixed in the back of the stator blade, respectively.

Fig. 3 shows that the computational domain is a cylinder ($12D_{r\max}$ in length and $5D_{r\max}$ in diameter) surrounding the pumpjet propulsor. The inlet is located $4D_{r\max}$ before the front face of pumpjet propulsor, and the outlet is situated $8D_{r\max}$ behind the front face of pumpjet propulsor. According to the operating feature of each component of pumpjet propulsor, the computational domain is divided into 3 parts, including the rotor domain, the stator domain and the external flow field domain, illustrated as Fig. 4. The computational cost of single working condition is approximately 7 h. The setting of the solution time is 400 iterations and the time step is $30/n \times \pi$. The residuals convergence history is shown as Fig. 5.

Table 1
Parameters of E779A propeller.

| | |
|---|---|
| Propeller diameter ($D_1$) | 227.3 mm |
| P/D ratio | 1.1 |
| Skew angle | 4°48″ |
| Rake | 4°3″ |
| Blade area ratio | 0.689 |
| Hub diameter ($D_H$) | 45.53 mm |

### 3.3. Computational grid of pumpjet propulsor

The quality of computational grid directly determines the accuracy and reliability of numerical prediction results. In this study, all the computational domains are filled with structured grids generated by ANSYS ICEM (2012), as shown in Fig. 6. In addition, in order to ensure the accuracy of tip clearance flow, the local grid in the tip clearance region has been refined. The number of entire computational domain grid is approximately $3.7 \times 10^6$, including $1.9 \times 10^6$ rotor domain grids and $1.0 \times 10^6$ stator domain girds. The minimum angles of the rotor domain and stator domain are 13° and 20°, which mainly appear in the region of blade tip and the boundary region between the hub and the blade.

### 3.4. Results and discussions

#### 3.4.1. Formation and development of tip clearance flows

The tip clearance size in this paper has been represented as a non-dimensional value which is defined as $\delta = (\text{Clearance size}/D_{r\max}) \times 100\%$. With the rotation of the rotor blade, there is an appearance of pressure difference between the suction side and the pressure side of the rotor blade, which is the one of the main reasons that leads to the formation of tip clearance flow, as shown in Fig. 7(a). Another main reason can be attributed to the relative rotation between the rotor blade and the inside wall of the duct, which causes a small fraction of the flows returns from the pressure side to the suction side, as shown in Fig. 7(b).

When the tip clearance flow goes through the tip clearance region, it is impacted by the viscosity force of the boundary layers. With the further development of tip clearance flow, the local low pressure regions come into sight in the tip clearance region and the rotor main flow region. Finally, the tip leakage vortex appears. The tip leakage vortex is mainly classified into two types: the Pressure Differential Vortex (PDV) caused by the pressure difference between the suction side and the pressure side of rotor blade in Fig. 8(a), the Sweeping Vortex (SV) caused by the discontinuity of the leading edge of the rotor blade in Fig. 8(b). As can be seen from Fig. 8(c), according to the location of the low pressure center, the PDV appears and attaches to the suction side of the rotor blade first, and then as the rotation of rotor blade, the low pressure center gradually separates from the suction side of the rotor blade and move to the rotor main flow along the inflow direction, and show the diffusion characteristic in the middle region of the main flow field of rotor. In addition, as illustrated in Fig. 8(c), the SV originates from the blade tip region of the leading edge and develops to the trailing edge in the tip clearance region. During the process of the SV transportation, a part of the SV continues to develop along the trailing edge direction, and at last merges with the main flow in the back-end region of the blade tip. The other part gradually separates from the tip clearance region, develops to the main flow field of rotor and finally mixes with the PDV and main flow in the main flow field of rotor. Comparing the development process and strength of the PDV and SV, it can be concluded that the main

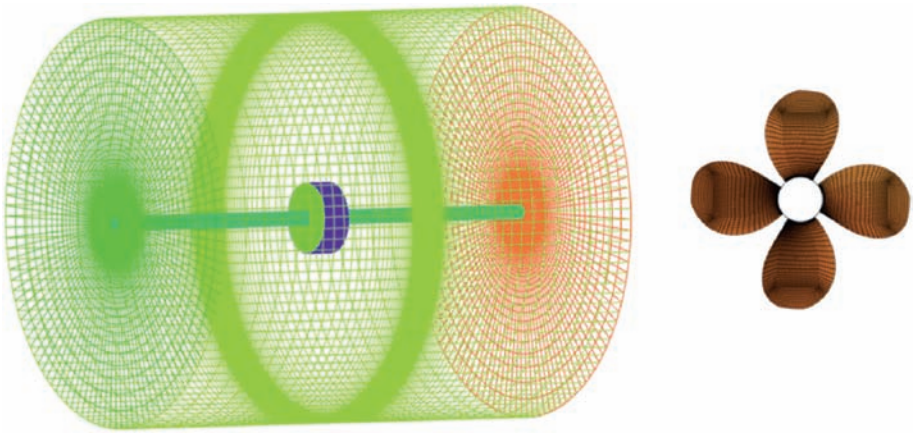

Fig. 1. Computational grid of E779A propeller.

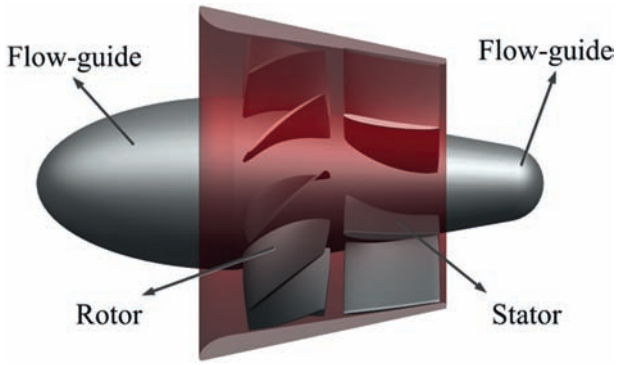


Fig. 2. Computational model of pumpjet propulsor.

Table 2
Parameters of the pumpjet propulsor.

| | |
|---|---|
| Numbers of rotor blade | 11 |
| Numbers of stator blade | 9 |
| Maximum diameter of rotor blade ($D_{rmax}$) | 250 mm |
| Minimum diameter of rotor blade ($D_{rmin}$) | 210 mm |
| Inlet diameter of duct ($D_{inlet}$) | 270 mm |
| Outlet diameter of duct ($D_{outlet}$) | 200 mm |
| Length of hub ($L_{hub}$) | 180 mm |

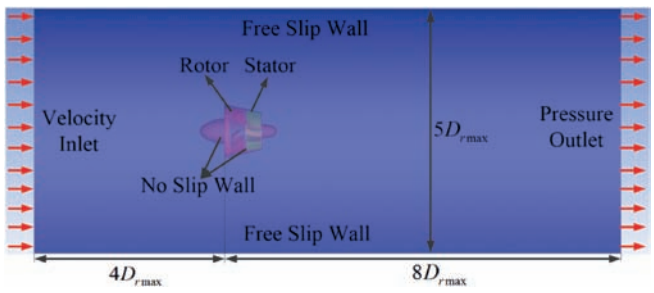


Fig. 3. Computational domain and boundary condition of pumpjet propulsor.

part of the tip leakage vortex is the PDV, and as the transportation of the PDV and SV, there must be accompanied by a strong energy exchange between the main flow and the tip leakage vortex, which results in an energy loss and a negative

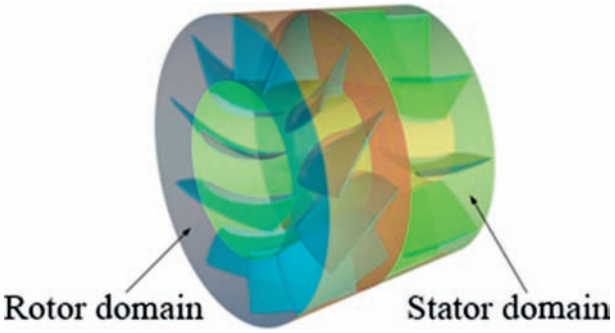


Fig. 4. Rotor and stator domains.

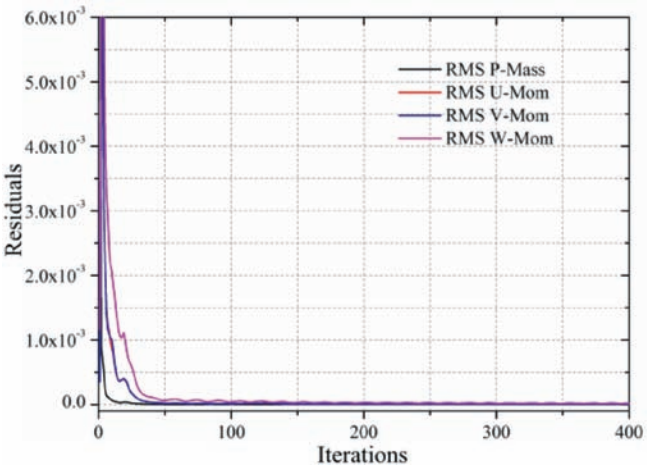


Fig. 5. Residuals convergence of simulations.

impact on the hydrodynamics and cavitation performance of the pumpjet propulsor.

### 3.4.2. Effect of tip clearance flow on the main flow

Fig. 9(a)–(f) show the radial distributions of three different velocity components (axial velocity $V_a$, tangential velocity $V_t$ and radial velocity $V_r$) with different Span along the axial direction. By analyzing and comparing the distribution characteristics of different velocity components, the following conclusions can be drawn:

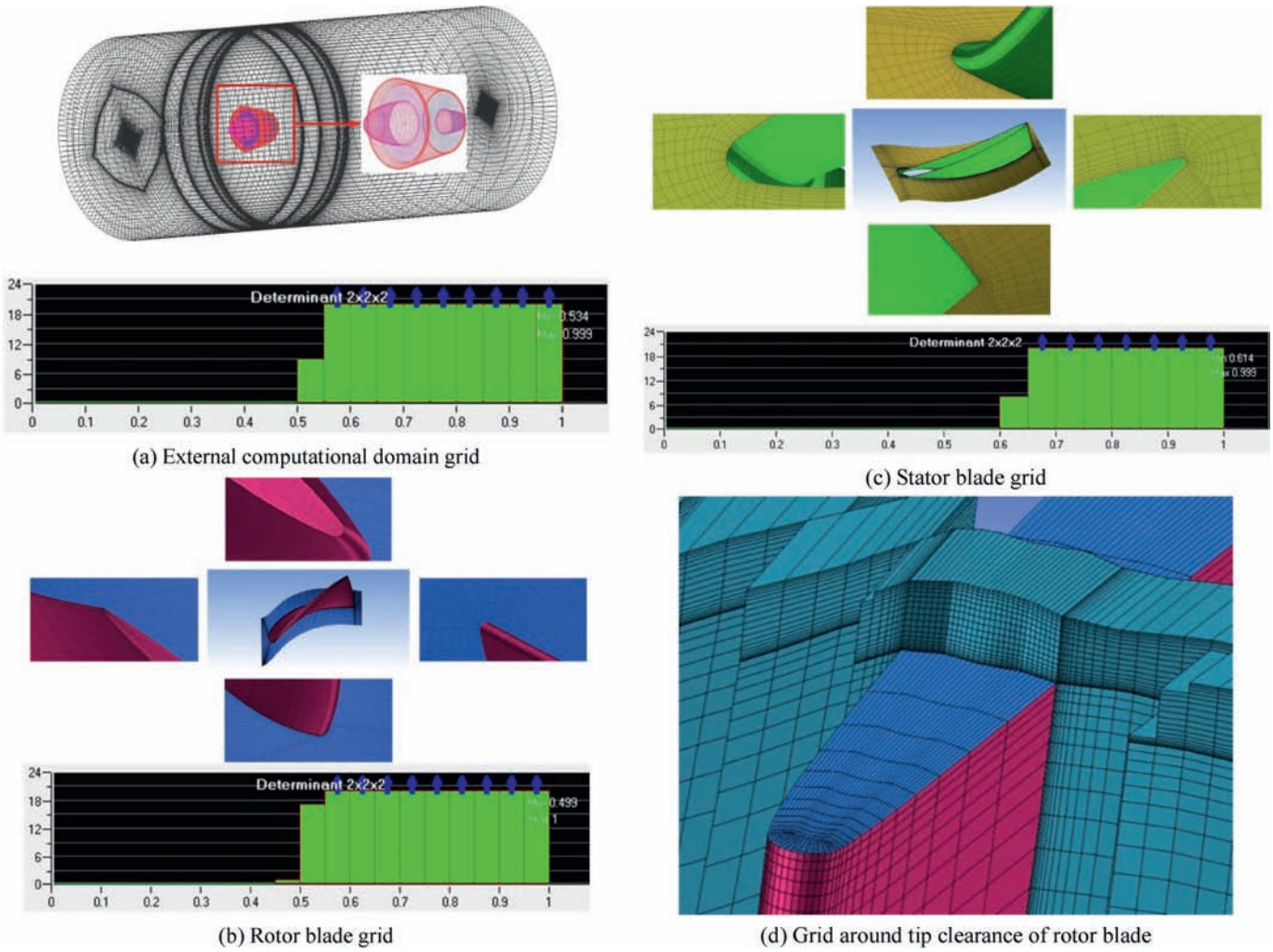


Fig. 6. Computational gird of pumpjet propulsor.

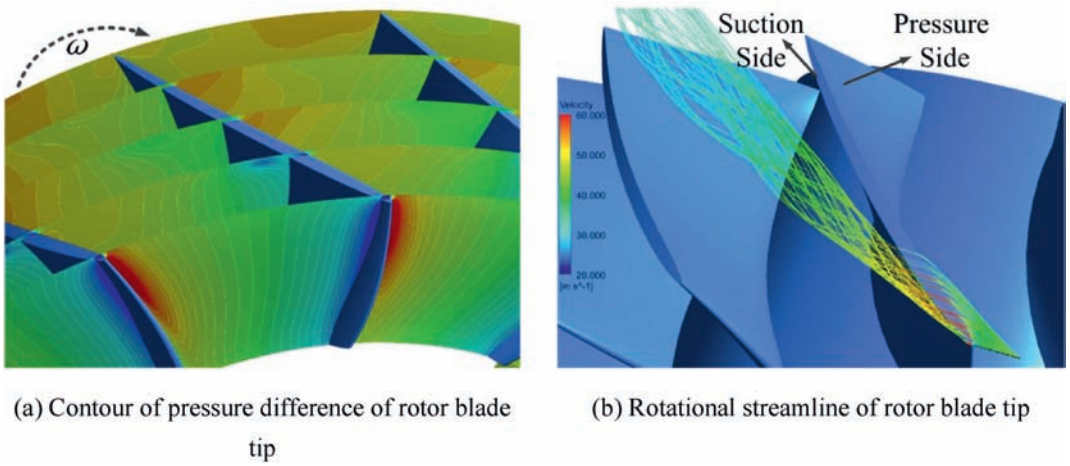


Fig. 7. Contours of pressure difference and rotational streamline of rotor blade tip.

For the front region of rotor domain, as shown in Fig. 9(a), $V_t$ and $V_r$ are basically unchanged with the increase of Span, while there is an obvious velocity gradient of $V_t$ near the hub region. That is mainly because the rotation of the guide-gap and hub gives rise to the rotation of the boundary layers that leads to the appearance of the increase of $V_t$. Simultaneously, the influence of the boundary layers causes the drop of $V_a$ near the hub region, but $V_a$ of other position increases with the

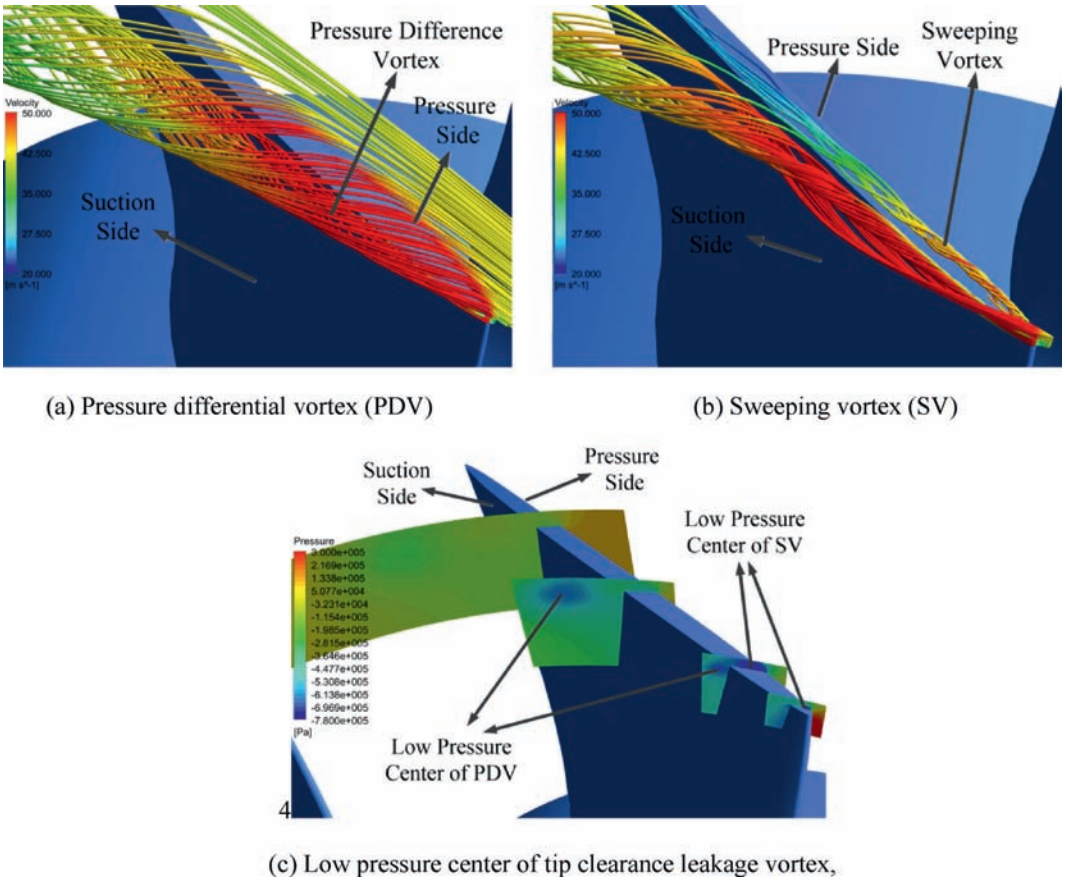


Fig. 8. Detailed structures of tip clearance leakage vortex.

increase of Span. Besides, because the flow of this region is mainly affected by the external flow, the flow of this region still maintains the features of the external flow, which results in a smaller trend of the increase of $V_a$.

For the region of rotor domain, as shown in Fig. 9(b), $V_a$ still occupies the dominant place and the increase trend is larger than that of the front region of rotor domain due to the rotational acceleration of rotor blade. However, $V_a$ and $V_r$ drop obviously near the tip clearance region. The reason for this phenomenon can be explained from two perspectives: (1) from the perspective of space, the rotor can be divided into two main regions: the rotor blade main flow region and the tip clearance flow region. The velocity level of the rotor blade main flow region is comparably high because of the rotation of the rotor blade. While the overall velocity of the tip clearance region is relatively low. So there must be a flow mass exchange between these two regions, namely, the high velocity fluid flow enters the low velocity fluid flow or the low velocity fluid flow goes into the high velocity fluid in a transitional region where the tip clearance region is located. (2) from the perspective of the boundary layers and the tip leakage vortex, the flow in the tip clearance region is mainly controlled by the viscous force of the boundary layers of the rotor blade tip and the inside wall of duct, which results in the decline of the velocity in this region. In addition, the local low pressure caused by the tip leakage vortex first appears in the region near the rotor blade tip of suction side. From the above analysis we know that there is an energy loss during the process of the transportation and development of the tip leakage vortex, which accounts for the weakening of the velocity components.

For the region between the rotor and stator, as shown in Fig. 9(c), the distribution trend of different velocity components in this region is roughly the same as that in the region of rotor domain. At the same time, $V_a$ and $V_r$ also reduce in the region near the blade tip clearance, which means the influence of the flow field of rotor domain has extended to the flow field between the stator and rotor. Furthermore, because the stator blade plays a role in stabilizing the flow fields, the decrease of each velocity component is lower than that of rotor domain.

For the region of stator domain and duct outlet, $V_a$ has a more significant accelerating gradient after the flow passes through the stator domain, which indicates that the stator blade cannot only stabilize the flow but also convert a portion of rotational kinetic energy to additional thrust. Meanwhile, $V_a$ in both regions drops in the area near the blade tip which illustrates that the influence generated by the tip clearance flow has spread all over the flow field inside the duct of pumpjet propulsor. The expansion of the influence scope of the tip clearance tip is very unfavorable to the performance and concealment of the pumpjet propulsor. Firstly, the reduction of the axial velocity implies that the thrust of the propulsor will be reduced in the axial direction. Furthermore, the

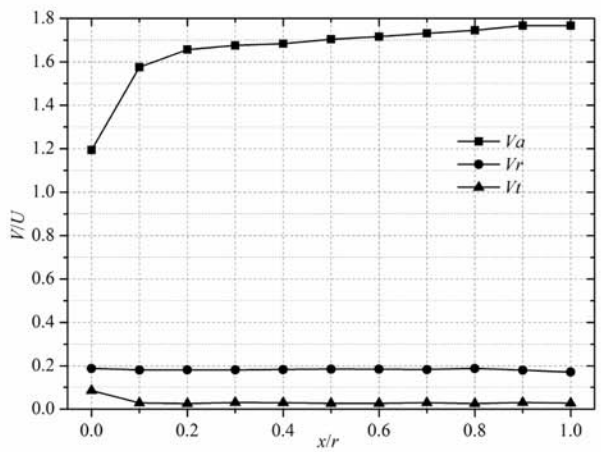


(a) Front region of rotor domain

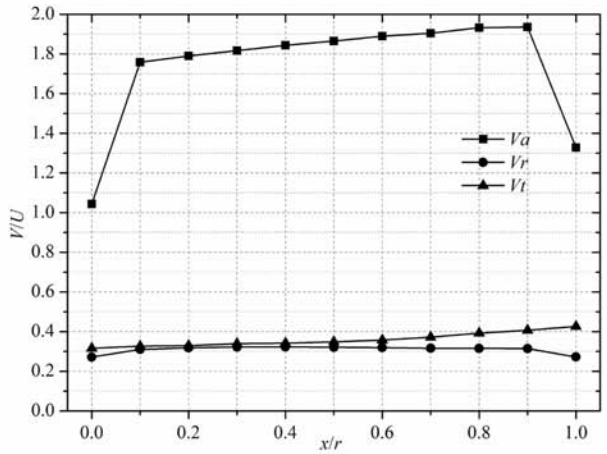


(b) Region of rotor domain

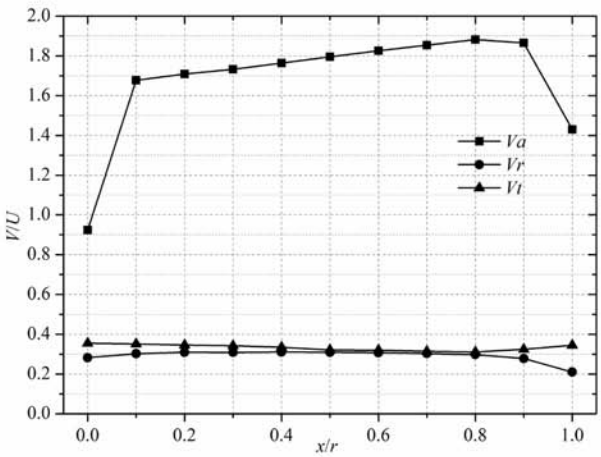


(c) Region between rotor and stator

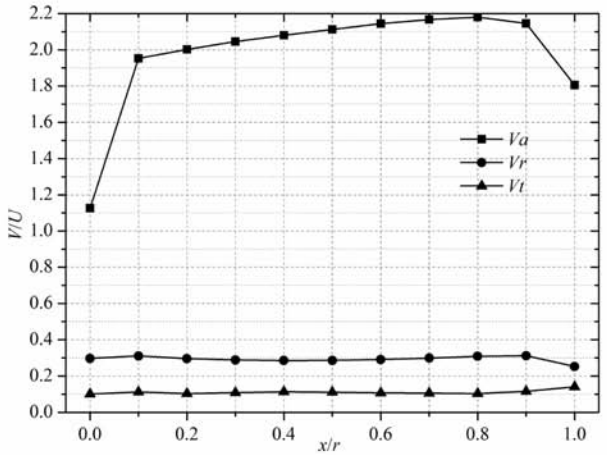


(d) Region of stator domain

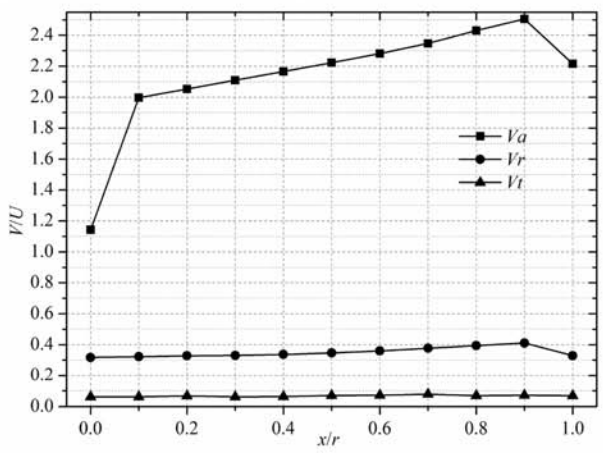


(f) Region of duct outlet

Fig. 9. Radial distributions of different velocity components with different span along the axial direction.

transportation and development of the tip leakage vortex caused by the tip clearance flow will result in the energy loss, while the local low pressure region of the vortex easily induces the occurrence of the cavitation noise and mechanical vibration, which will cause negative impact on the concealment of the pumpjet propulsor.

*3.4.3. Effect of tip clearance size on the pumpjet propulsor performance*

In Figs. 10 and 11, the velocity contours and streamlines in the tip clearance region with different $\delta$ are presented. As can be concluded from the contours, the velocity distributions with different $\delta$ are the same in general: The velocity close to the leading edge of the blade tip is higher than that close to the trailing edge due to the rotation of the rotor blade. Meanwhile, the velocity distributions in tip clearance region with different $\delta$ have their own features in details: The low velocity area is mainly focus on the trailing edge and has not affected the velocity distribution of the adjacent blade tip at $\delta = 0.5\%$. As for $\delta = 1\%$, the low velocity area increases significantly and even spreads to the rear region of the adjacent blade tip. The reasons for the above phenomenon can be summarized as: as for the smaller tip clearance size, the flows are strongly impacted by the viscous force of the boundary layers. The tip clearance flows cannot possess enough space for the development and transportation, and then the tip leakage vortex has a lower intensity and is less mixed with the main flow, of which interference to the main flow field is not strong. As for the larger tip clearance size, there has enough space for the tip clearance flow to develop and transport and then the strength and area of the tip leakage vortex is enlarged which has obvious influence on the main flow field and even the flow field of the adjacent blade. Combined with the tip leakage vortex streamlines in Fig. 11(a) and (b), it can be found that the strength of the tip vortex is relatively weak and the dissipation is shown at the downstream under the condition of $\delta = 0.5\%$. While as for $\delta = 1\%$, the vortex is not completely dissipated at the downstream. The vortex intensity has a more significant improvement, and the area of the vortex has nearly extended to the suction side of the adjacent blade which is consistent with Fig. 10.

Fig. 12 shows the curves of the cavitation area ratio ($A$) of $\delta = 0.5\%$ and $\delta = 1.0\%$, respectively, which indicates the variation of the cavitation area along the radial direction with different rotational speed, $x$ denotes the radius of the monitoring position and $r$ represents the rotor radius. As can be seen from Fig. 12, for two different tip clearance sizes, the cavitation area increases at the lower radius, while in the tip clearance region, the cavitation area first decreases and then increases. The difference of the cavitation area between $\delta = 0.5\%$ and $\delta = 1.0\%$ is not great under the circumstance of lower radius. The cavitation area of $\delta = 1.0\%$ has a more significant increment than that of $\delta = 0.5\%$ under the condition of high rotational speed. Simultaneously, the location of the increment of $\delta = 0.5\%$ is closer to the blade tip than that of $\delta = 1.0\%$. The primarily reason is that the tip leakage vortex caused by the tip clearance flow mainly develops and transports along the axial and tangential direction. But in the radial direction, the development of the tip clearance vortex is not enough, which has little effect on the main flow field of the rotor blade. Thereby, it is shown that the difference of the cavitation area between $\delta = 0.5\%$ and $\delta = 1.0\%$ is relatively small at lower radius. However, in the tip clearance region, the tip leakage vortex leads to the occurrence of the local low pressure region which accounts for the generation of the tip leakage cavitation and then makes the increment of the cavitation area. In addition, the tip clearance flow is able to be more fully developed under the situation of $\delta = 1.0\%$ and its influence area has been improved, which causes that the increment of the cavitation area of $\delta = 1.0\%$ is more far away from the blade tip.

In Figs. 13 and 14, the contours of the rotor blade cavitation and tip clearance cavitation of $\delta = 0.5\%$ and $\delta = 1.0\%$ have been presented. As illustrated in figures, the cavitation area and intensity is improving with the increasing of the tip clearance size, which partly explains that the cavitation area of $\delta = 1.0\%$ has a more significant increment than that of $\delta = 0.5\%$, as shown in Fig. 12. Comparing Fig. 13(a) with (b),

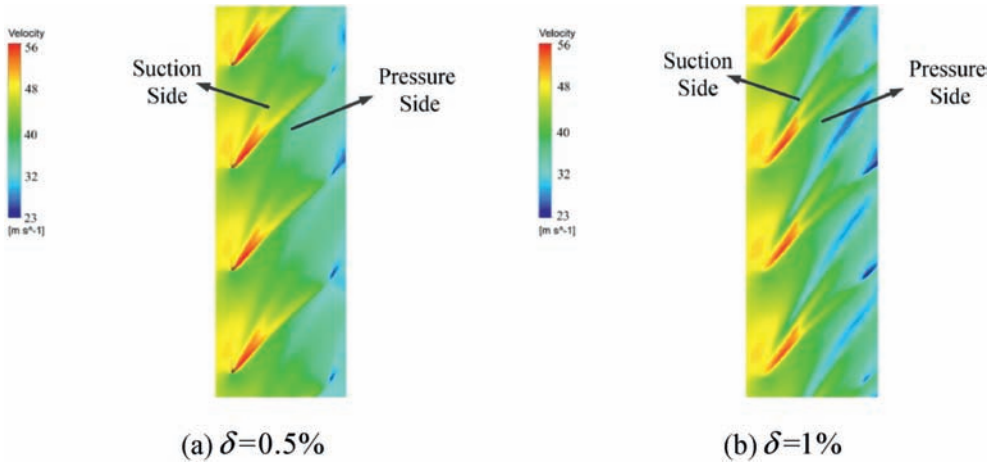


Fig. 10. Velocity contours in the tip clearance region with different $\delta$.

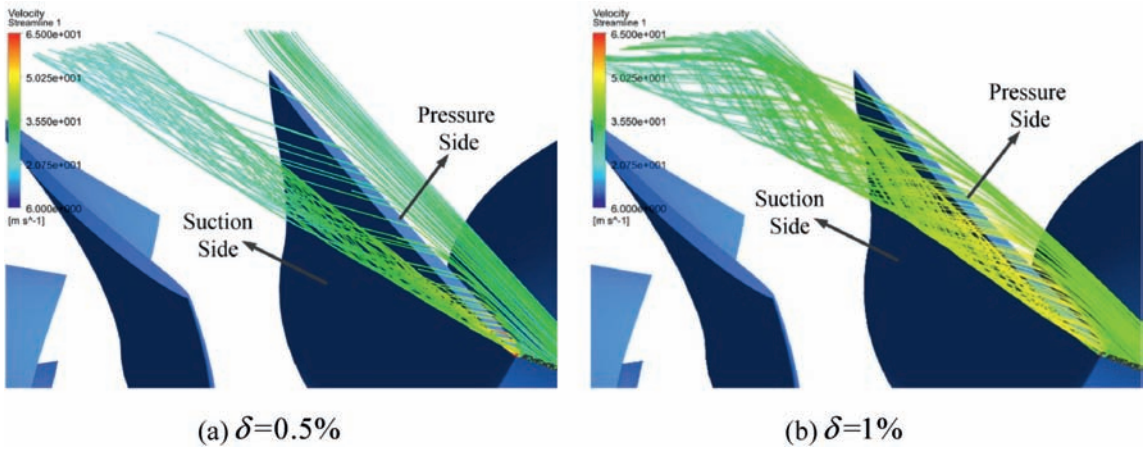


Fig. 11. Velocity streamlines in the tip clearance region with different $\delta$.

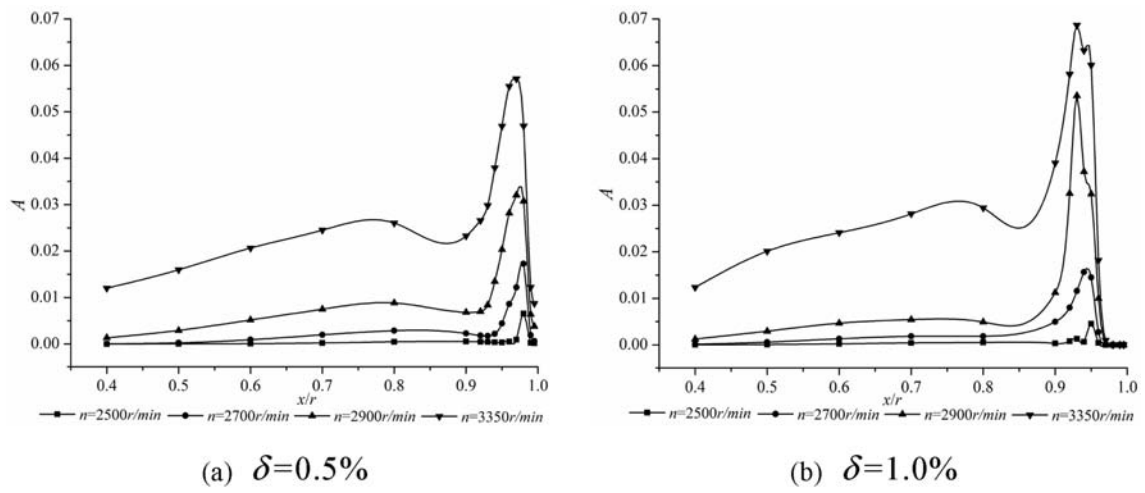


Fig. 12. Curves of cavitation area ratio of $\delta = 0.5\%$ and $\delta = 1.0\%$.

it can be found that there is a distinct boundary between the tip clearance cavitation and the rotor blade cavitation of $\delta = 0.5\%$. This phenomenon can be attributed to the smaller tip clearance which makes that the flows in the tip clearance region have been squeezed and the tip clearance leakage vortex is not able to possess the sufficient development. With the increase of the tip clearance size, as shown in Fig. 14(b), the boundary has gradually disappeared, and the location of

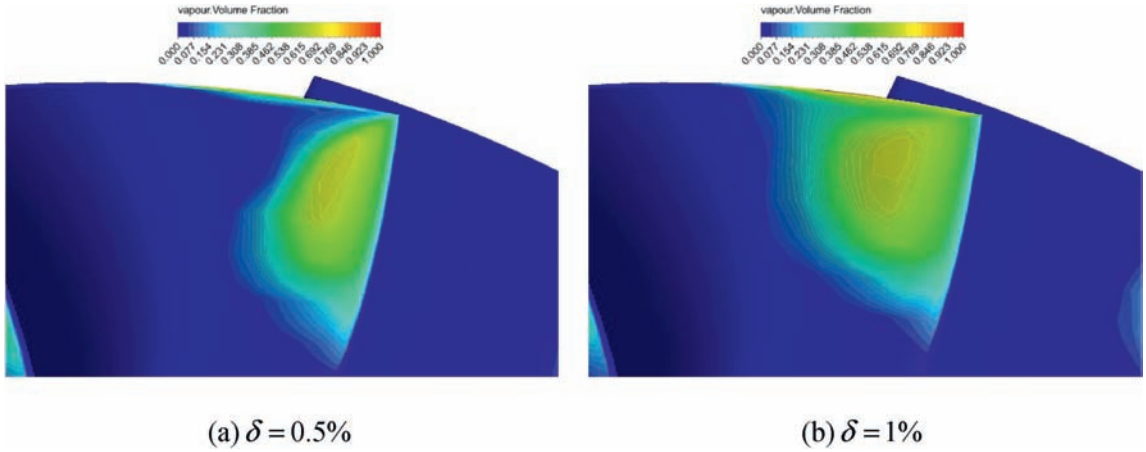


Fig. 13. Contours of the rotor blade cavitation of $\delta = 0.5\%$ and $\delta = 1.0\%$.

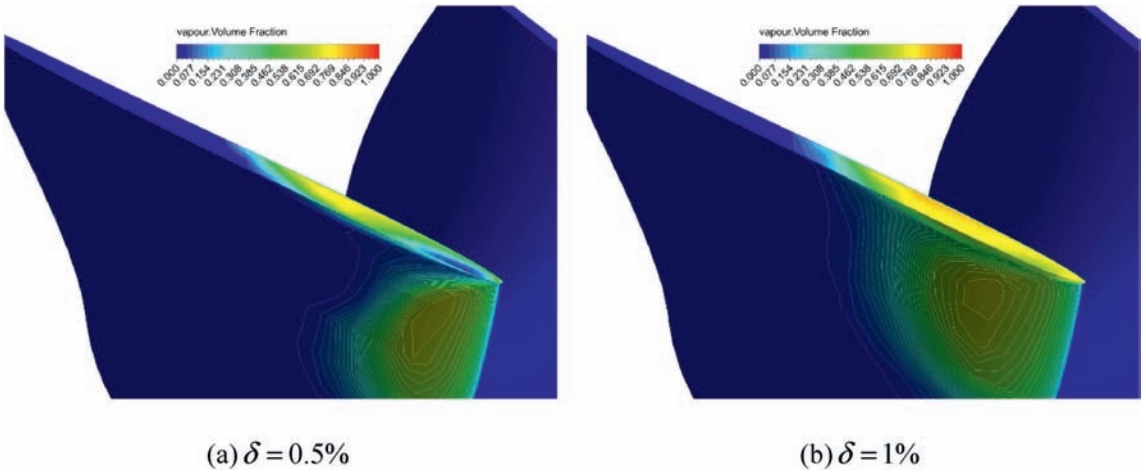


Fig. 14. Contours of the tip clearance cavitation of $\delta = 0.5\%$ and $\delta = 1.0\%$.

the maximum intensity of the tip clearance cavitation and rotor blade cavitation has developed to the trailing edge direction, which indicates that the tip clearance size has a direct influence on the cavitation distribution of the pumpjet propulsor.

## 4. Conclusions

In this study, the tip clearance flow characteristics of a pumpjet propulsor based on CFD method have been investigated. The Z-G-B cavitation model based on the RANS method and the structure grids have been employed.

The formation and development of the tip clearance flows has been investigated and presented. The structure of the tip leakage vortex has been shown. Results show that the tip leakage vortex is mainly classified into two types: the Pressure Differential Vortex (PDV) caused by the pressure difference between the suction side and the pressure side of the rotor blade and the Sweeping Vortex (SV) caused by the sheer effect and the discontinuity of the leading edge of the rotor blade. Comparing the development process and strength of the PDV and SV, it can be concluded that the main part of the tip leakage vortex is the PDV, and as the transportation of the PDV and SV, there must be accompanied by a strong energy exchange between the main flow and the tip leakage vortex, which results in an energy loss and a negative impact on the hydrodynamics and cavitation performance of the pumpjet propulsor.

The radial distributions of three different velocity components with different Span along the axial direction have been carried out to present the influence of the tip clearance flow on the main flow. Results show that the velocity near the tip clearance region drops obviously due to the impact of the tip clearance leakage. Simultaneously, the stator blade plays a role in stabilizing the flow fields and reducing the negative influence generated by the tip clearance leakage. In addition, by comparing the velocity distributions of different axial position, it can be found that the influence generated by the tip clearance flow has spread all over the flow field inside the duct of the pumpjet propulsor. The expansion of the influence scope of the tip clearance tip is very unfavorable to the performance and the concealment of the pumpjet propulsor.

The influences of the tip clearance size on the pumpjet propulsor performance have been presented. As can be concluded from the results, with the increase of $\delta$, there has enough space for the tip clearance flow to develop and transport and then the strength and area of the tip leakage vortex is enlarged which has obvious influence on the main flow field and even the flow field of the adjacent blade. The strength of the tip vortex is relatively weak and the dissipation is shown at the downstream under the condition of $\delta = 0.5\%$. While as for $\delta = 1\%$, the vortex is not completely dissipated at the downstream. The vortex intensity has a more significant improvement. Furthermore, the difference of the cavitation area between $\delta = 0.5\%$ and $\delta = 1.0\%$ is not great under the circumstance of lower radius. While the cavitation area of $\delta = 1.0\%$ has a more significant increment than that of $\delta = 0.5\%$, especially for the high rotational speed. Simultaneously, the location of the increment of $\delta = 0.5\%$ is closer to the blade tip than that of $\delta = 1.0\%$. The tip clearance size has a direct influence on the cavitation distribution of the pumpjet propulsor.

## Acknowledgment

This work is supported by the National Natural Science Foundation of China [Grant No. 51175481] and Science Research Foundation of North University of China [Grant No. 2017002].

## References

ANSYS, 2012. ANSYS CFX and ICEM Release 14.5. ANSYS Inc, Canonsburg (PA).

Arazgaldi, R., Hajilouy, A., Farhanieh, B., 2009. Experimental and numerical investigation of marine propeller cavitation. Scientia Eranica Trans. B Mech. Eng. 16 (6), 525–533.

Brennen, C.E., 2013. A review of the dynamics of cavitating pumps. ASME J. Fluids Eng. 135 (6), 061301.

Cheah, K.W., Lee, T.S., Winoto, S.H., Zhao, Z.M., 2007. Numerical flow simulation in a centrifugal pump at design and off-design conditions. Int. J. Rotat. Mach. 2007 http://dx.doi.org/10.1155/2007/83641.

Ivanell, S., 2001. Hydrodynamic Simulation of a torpedo with Pump Jet Propulsion System. Royal Institute of Technology, Stockholm, Sweden, p. 77 (Master thesis).

Ji, B., Luo, X., Wu, Y., Liu, S., Xu, H., Oshima, A., 2010. Numerical investigation of unsteady cavitating turbulent flow around a full scale marine propeller. J. Hydrodyn. Ser. B 22 (5), 747–752.

Ji, B., Luo, X., Wu, Y., 2014a. Unsteady cavitation characteristics and alleviation of pressure fluctuations around marine propellers with different skew angles. J. Mech. Sci. Technol. 28 (4), 1339–1348.

Ji, B., Luo, X., Arndt, R.E., Wu, Y., 2014b. Numerical simulation of three dimensional cavitation shedding dynamics with special emphasis on cavitation–vortex interaction. Ocean Eng. 87, 64–77.

Ji, B., Luo, X.W., Arndt, R.E., Peng, X., Wu, Y., 2015. Large eddy simulation and theoretical investigations of the transient cavitating vortical flow structure around a NACA66 hydrofoil. Int. J. Multiph. Flow 68, 121–134.

Ji, B., Long, Y., Long, X.P., Qian, Z.D., Zhou, J.J., 2017. Large eddy simulation of turbulent attached cavitating flow with special emphasis on large scale structures of the hydrofoil wake and turbulence-cavitation interactions. J. Hydrodyn. Ser. B 29 (1), 27–39.

Li, D., Grekula, M., Lindell, P., Hallander, J., 2012. Prediction of cavitation for the INSEAN propeller E779A operating in uniform flow and non-uniform wakes. In: Proceedings of the 8th International Symposium on Cavitation. Singapore, pp. 368–373.

Lindau, J.W., Boger, D.A., Medvitz, R.B., Kunz, R.F., 2005. Propeller cavitation breakdown analysis. J. Fluids Eng. 127 (5), 995–1002.

Liu, Y., Zhao, P., Wang, Q., Chen, Z., 2012. URANS computation of cavitating flows around skewed propellers. J. Hydrodyn. Ser. B 24 (3), 339–346.

Lu, L., Pan, G., Sahoo, P.K., 2016. CFD prediction and simulation of a pumpjet propulsor. Int. J. Nav. Arch. Ocean Eng. 8 (1), 110–116.

Luo, X.W., Bin, J.I., Tsujimoto, Y., 2016. A review of cavitation in hydraulic machinery. J. Hydrodyn. 28 (3), 335–358.

Morgut, M., Nobile, E., 2012. Numerical predictions of cavitating flow around model scale propellers by CFD and advanced model calibration. Int. J. Rotat. Mach. 2012 http://dx.doi.org/10.1155/2012/618180.

Muscari, R., Di Mascio, A., 2011. Numerical simulation of the flow past a rotating propeller behind a hull. In: Proceedings of the 2nd International Symposium on Marine Propulsors. Hamburg, Germany, June.

Pan, G., Lu, L., 2016. Numerical simulation of unsteady cavitating flows of pumpjet propulsor. Ships Offshore Struct. 11 (1), 64–74.

Park, W., Jang, J.H., Chun, H.H., Kim, C.M., 2005. Numerical flow and performance analysis of waterjet propulsion system. Ocean Eng. 32 (14–15), 1740–1761.

Rhee, S.H., Joshi, S., 2005. Computational validation for flow around a marine propeller using unstructured mesh based Navier-Stokes solver. JSME Int. J. Ser. B 48 (3), 562–570.

Salvatore, F., Streckwall, H., Van Terwisga, T., 2009. Propeller cavitation modelling by CFD-results from the VIRTUE 2008 Rome workshop. In: Proceedings of the First International Symposium on Marine Propulsors, Trondheim, Norway, June.

Shin, K.W., 2010. Cavitation Simulation on Marine Propellers. Technical University of Denmark, Copenhagen.

Singhal, A.K., Athavale, M.M., Li, H., Jiang, Y., 2002. Mathematical basis and validation of the full cavitation model. T ASME J. Fluids Eng. 124 (3), 617–624.

Suryanarayana, C., Satyanarayana, B., Ramji, K., Saiju, A., 2010a. Experimental evaluation of pumpjet propulsor for an axisymmetric body in wind tunnel. Int. J. Nav. Arch. Ocean Eng. 2 (1), 24–33.

Suryanarayana, C., Satyanarayana, B., Ramji, K., Saiju, A., 2010b. Performance evaluation of an underwater body and pumpjet by model testing in cavitation tunnel. Int. J. Nav. Arch. Ocean Eng. 2 (1), 57–67.

Suryanarayana, C., Satyanarayana, B., Ramji, K., Rao, M.N., 2010c. Cavitation studies on axi-symmetric underwater body with pumpjet propulsor in cavitation tunnel. Int. J. Nav. Arch. Ocean Eng. 2 (4), 185–194.

Watanabe, T., Kawamura, T., Takekoshi, Y., Maeda, M., Rhee, S.H., 2003. Simulation of steady and unsteady cavitation on a marine propeller using a RANS CFD code. In: Proceedings of 5th International Symposium on Cavitation, Osaka, Japan, November.

Zhang, D., Shi, W., Chen, B., Guan, X., 2010. Unsteady flow analysis and experimental investigation of axial-flow pump. J. Hydrodyn. Ser. B 22 (1), 35–43.

Zhu, Z., Fang, S., 2012. Numerical investigation of cavitation performance of ship propellers. J. Hydrodyn. Ser. B 24 (3), 347–353.